



# Construction of dual-channel for optimizing Z-scheme photocatalytic system

Lulu Zhang, Wenhui Feng, Bo Wang, Kaiqiang Wang, Fan Gao, Yan Zhao, Ping Liu\*

Research Institute of Photocatalysis, State Key Laboratory of Photocatalysis on Energy and Environment, Fuzhou University, Fuzhou, 350002, PR China

## ARTICLE INFO

### Article history:

Received 17 January 2017

Received in revised form 17 March 2017

Accepted 19 April 2017

Available online 22 April 2017

### Keywords:

Dual-channel

Z-scheme

Facet

Visible light photocatalysis

## ABSTRACT

A ternary all-solid-state visible-light Z-scheme photocatalytic system  $\text{BiVO}_4/\text{Au}@\text{CdS}$  is prepared by means of a two-step route, which is selectively built on the  $\{010\}$  facet of  $\text{BiVO}_4$  crystals in this system. Vectorial migration of photogenerated charge carriers through two order transmission channels in Z-scheme photocatalytic system further prolongs the mean free path of electrons, realizing effective separation of photogenerated charge carriers and possesses high redox ability. As expected, such  $\text{BiVO}_4/\text{Au}@\text{CdS}$  Z-scheme photocatalytic system exhibits highly efficient photocatalytic performance. Our current work is expected to offer new insight into construction of dual separation channels for rational design and compound of photocatalyst with high performance.

© 2017 Published by Elsevier B.V.

## 1. Introduction

In the past decades, semiconductor photocatalysis as a promising and eco-friendly technology has attracted extensive attention due to the energy shortages and environmental crisis problem [1–6]. Owing to the limitation of narrow light responsive range and fast recombination rate of photogenerated charge carriers [7–11], photocatalytic technology doesn't achieve breakthrough in term of its practical application. Therefore, it is extremely urgent to develop visible-light-responsive photocatalysts with superior carrier separation efficiency.

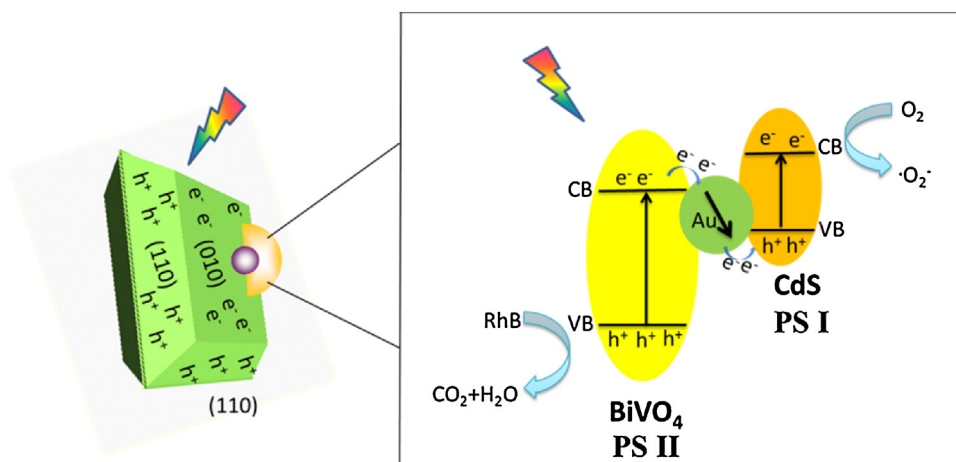
As known, the so-called Z-scheme photocatalytic process resembles natural photosynthesis which is the most important light-dependent reaction in nature. Both of photosynthesis and Z-scheme photocatalytic process include electrons (or energy) exchange among various functional components and energy transfer at the interface. Although natural photosynthesis undergoes a series of photo-induced species transmission among nanoscale architectures generally containing light-harvesting complexes, protein–metal clusters and a group of redox biocatalysts, it still can achieve high conversion efficiency. A crucial factor is the efficient electronic energy-transfer from the photo-excited chromophores to the catalytic clusters for chemical reactions [12], which is based on the accurate assemble of various functional components assuring energy transfer in an orderly way. Therefore, an efficient

photochemical system could be achieved by selecting appropriate components. Artificial Z-scheme photocatalytic system contains the photosystem I and II (hereafter referred to as PS I and PS II), as shown in Scheme 1 [13]. In Z-scheme photocatalytic process, the photogenerated electrons transfer from the conduction band (CB) of PS II to the valence band (VB) of PS I [14–17]. On one hand, the separation efficiency of photogenerated carriers can be improved through carriers transfer at the interface. On the other hand, separated electrons or holes possess higher redox ability, which is more beneficial to involve in related reactions. Therefore Z-scheme photocatalytic system has great potential to effectively utilize solar energy. In the case of artificial Z-scheme photocatalytic system, however, the complicated interfacial environment may lead to serious energy lose (low transfer rate of carriers [18,19] and opposite charge carriers accumulate at the surface [17,20]), resulting the efficiency of artificial Z-scheme photocatalytic system far away from the theoretical conversion efficiency. Thus, developing an efficient strategy to relieve the above-mentioned issues becomes a key step for optimizing the energy utilization efficiency of Z-scheme photocatalytic system.

Fortunately, some previous studies have proved that introducing electron mediators (including Au [21–23], Ag [16,24,25], reduced graphene oxide [26] and so on) at the interface between PS I and PS II could reduce the transmission impedance of electrons and improve electron transfer rate across the interface, in which electron mediators act as a transfer channel for carriers. Regrettably, because free electron and hole are photo-excited simultaneously at the surface of PS I or PS II, and the isotropic migration of photo-induced electron–hole pairs from the bulk to

\* Corresponding author.

E-mail address: [liuping@fzu.edu.cn](mailto:liuping@fzu.edu.cn) (P. Liu).



**Scheme 1.** The proposed mechanism of photodegradation of RhB by  $\text{BiVO}_4/\text{Au}@\text{CdS}$  under visible light irradiation.

surface of each semiconductor, opposite charge carriers can accumulate inevitably in the surface and its density will gradually increase, inducing serious surface self-recombination [20]. It's not difficult to imagine that surface self-recombination would be suppressed if extra pre-screening procedure is integrated in PS II to assure photogenerated electrons are selectively collected on the PS II. Alternatively, as we know, crystal facet engineering of various semiconductors ( $\text{TiO}_2$  [10,27],  $\text{BiVO}_4$  [28–30],  $\text{ZnO}$  [31],  $\text{WO}_3$  [32],  $\text{BiOI}$  [33]) could provide a new opportunity to drive free electrons/holes to the specific facets in PS II, due to the differences in the energy levels in the conduction band (CB) and valence band (VB) between two specific facets, achieving spatial charge separation. Namely, the photogenerated electrons transfer from a facet with more negative CB potential to another facet, while holes transfer in the opposite direction to the facet with more negative CB potential in PS II. In this case, facet engineering can act as a separation channel. Therefore, a predictive model, in which PS I is rationally arranged on the electron-gathered facets in PS II with a function of facet engineering collector and metal nanostructure embedding in the interface between PS II and PS I, is expected to be an integration of separation channel and transfer channel to improve energy transfer rate and decrease serious energy lose in the interface. Besides, this predictive system should be integration between the complementarities of interfacial composite engineering and crystal facet engineering. On one hand, interfacial metal nanostructure may transfer electron from PS II to PS I to maintain the constant potential difference between two facets. On the other hand, electrons gathering caused by facet-driving could provide more transferable electrons owing to suppression of bulk and surface self-recombination in PS II.

In order to realize the above project, the first thing is to choose a photocatalyst PS II with special facets. As a promising visible-light driving semiconductor photocatalyst, monoclinic bismuth vanadate ( $\text{m-BiVO}_4$ ) has attracted considerable attention due to its narrow band gap, good chemical and thermal stability, non-toxicity and good photocatalytic performance under visible light irradiation [30,34,35]. Recent studies confirmed that the conduction band edge and valence band edge of the  $\{110\}$  facet of  $\text{m-BiVO}_4$  are 0.42 and 0.37 eV respectively, which is higher than those of its  $\{010\}$  facet. The difference of individual energy band levels between  $\{110\}$  and  $\{010\}$  facets leads to the migration of holes and electrons to different facet, respectively [28,29]. Therefore,  $\text{BiVO}_4$  with special facets is chosen as the PS II in Z-scheme photocatalytic system. Au can be chosen as a transmission channel to transfer electrons. Besides, Au nanoparticle also can be an anchor for depositing CdS onto Au nanoparticle due to the strong affinity of Au atoms to sulphur [36].

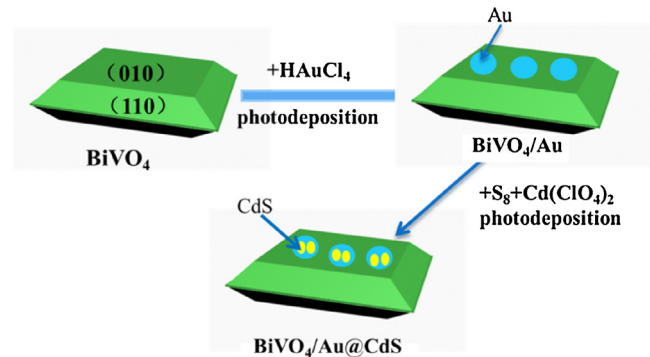


**Fig. 1.** Schematic of the preparation route of  $\text{BiVO}_4/\text{Au}@\text{CdS}$  Z-scheme photocatalytic system through a two-step process.

CdS with suitable band gap energy can be as the PS I in Z-scheme photocatalytic system.

Here, we report the all-solid-state visible-light Z-scheme photocatalytic system  $\text{BiVO}_4/\text{Au}@\text{CdS}$ , which is selectively built on the  $\{010\}$  facet of  $\text{BiVO}_4$  crystals in this system. The schematic of the preparation route of the Z-scheme photocatalytic system is given in Fig. 1. Au nanoparticles only distribute on the  $\{010\}$  facets of  $\text{BiVO}_4$  crystals by facile photo-deposition method. The growth of CdS is initialized by illuminating the suspension containing the prepared  $\text{Au/BiVO}_4$ , S and  $\text{Cd}(\text{ClO}_4)_2$ . Under irradiation, S molecules are reduced to  $\text{S}^{2-}$  ions, which then selectively adsorbed on the surface of Au. The  $\text{S}^{2-}$  ions react with  $\text{Cd}^{2+}$  and form CdS, so that the CdS nanoparticles are naturally formed onto the surfaces of the Au nanoparticles [3,18,22]. The photocatalytic activity is investigated by photo-degradation organic dye. Such the Z-scheme photocatalytic system by means of meticulous design possesses the highest photocatalytic performance. Our current work is expected to offer new insight into the construction of multiple separation channels for rational design and synthesis of photocatalyst with high activity.

## 2. Experimental

### 2.1. Preparation

#### 2.1.1. Materials

Bismuth nitrate pentahydrate ( $\text{Bi}(\text{NO}_3)_3 \cdot 5\text{H}_2\text{O}$ , >99.0%), ammonium vanadate ( $\text{NH}_4\text{VO}_3$ , >99.0%), ammonia water ( $\text{NH}_3 \cdot \text{H}_2\text{O}$ , 25–28 wt%), nitric acid ( $\text{HNO}_3$ , 65–68 wt%), gold chloride ( $\text{HAuCl}_4 \cdot 4\text{H}_2\text{O}$ ), absolute ethanol and cadmium sulfide (CdS)

are purchased from Sinopharm Chemical Reagent Co., Ltd. (Shanghai, China). Sulfur and cadmium perchlorate hexahydrate ( $\text{Cd}(\text{ClO}_4)_2 \cdot 6\text{H}_2\text{O}$ ) are obtained from Alfa Aesar, USA. Deionized (DI) water is used throughout this study. All reagents are used directly without further purification.

### 2.1.2. Synthesis of $\text{BiVO}_4$

$\text{BiVO}_4$  with  $\{110\}$  and  $\{010\}$  facets exposed is synthesized by a hydrothermal procedure [28]. Typically, 36 mmol  $\text{Bi}(\text{NO}_3)_3 \cdot 5\text{H}_2\text{O}$  and equal amount of  $\text{NH}_4\text{VO}_3$  are dissolved into 300 mL  $\text{HNO}_3$  solution (2 M) and the pH value of the solution is then adjusted to 2.0 with ammonia solution under stirring until formation of an orange precipitate. After about 2 h aging, the orange precipitate at the bottom of the beaker is transferred to a 100 mL Teflon-lined stainless steel autoclave and heated at 200 °C for 24 h and then allow it cool down. A vivid yellow powder is separated by filtration, washed with DI water for several times. Then the products are dried at 60 °C overnight in vacuum oven.

### 2.1.3. Synthesis of $\text{BiVO}_4/\text{Au}$

$\text{BiVO}_4/\text{Au}$  sample is prepared by photoreduction method. 500 mg  $\text{BiVO}_4$  is added to 100 mL of DI water and stirred. Then, a certain amount of 0.05 M  $\text{HAuCl}_4$  trihydrate is added. The suspension is then bubbled with nitrogen for 1 h in the dark, followed by the irradiation with a 300 W Xe lamp and a 420 nm UV cut-off filter for 20 min to achieve  $\text{Au}/\text{BiVO}_4$ . The products are centrifugally separated and washed several times with DI water, then heat at 60 °C overnight.

### 2.1.4. Synthesis of $\text{BiVO}_4/\text{Au}@\text{CdS}$

200 mg prepared  $\text{BiVO}_4/\text{Au}$  is dissolved in 30 mL 50% ethanol aqueous solution, stirring for a few minutes at room temperature. Subsequently, a suitable amount of S and  $\text{Cd}(\text{ClO}_4)_2 \cdot 6\text{H}_2\text{O}$  is added in the above solution and bubbled with nitrogen for 30 min in the dark, irradiation is carried out for a given period with a 300W Xe lamp and a 420 nm UV cut-off filter. Then, the precipitate is harvested by centrifugation and washed several times with deionized water before being dried in oven at 60 °C.

### 2.1.5. Synthesis of $\text{BiVO}_4/\text{CdS}$

$\text{BiVO}_4/\text{CdS}$  is synthesized using the same method as synthesis of  $\text{BiVO}_4/\text{Au}@\text{CdS}$  samples, but instead of  $\text{BiVO}_4/\text{Au}$  by  $\text{BiVO}_4$ .

### 2.1.6. Synthesis of $\text{BiVO}_4/\text{CdS}/\text{Au}$

$\text{BiVO}_4/\text{CdS}/\text{Au}$  is synthesized using the same method as synthesis of  $\text{BiVO}_4/\text{Au}$  samples, but instead of  $\text{BiVO}_4$  by  $\text{BiVO}_4/\text{CdS}$ .

### 2.1.7. Synthesis of $\text{BiVO}_4$ -Particles

$\text{BiVO}_4$  particles, without  $\{110\}$  and  $\{010\}$  facets exposed, are synthesized by a hydrothermal procedure. Typically, 8 mmol of  $\text{Bi}(\text{NO}_3)_3 \cdot 5\text{H}_2\text{O}$  is dissolved in 30 mL ethylene glycol to form solution A and 8 mmol of  $\text{NH}_4\text{VO}_3$  is dissolved in 30 mL deionized water to form solution B. Then the solution B is slowly dropped into the solution A under vigorous stirring to form a bisque mixture. The pH value of the solution is then adjusted to 5.0 with 2 M  $\text{NaOH}$  aqueous solution under stirring until formation of an orange precipitate. After about 30 min stirring, the mixture is finally transferred into a 100 mL Teflon-lined stainless steel autoclave and heated at 180 °C for 24 h and then allowed it cool down. The products are separated by filtration, washed with DI water and absolute ethanol for several times. Then the products are dried at 60 °C overnight in vacuum oven. This sample is denoted by  $\text{BiVO}_4$ -P.

### 2.1.8. Synthesis of $\text{BiVO}_4/\text{Au}@\text{CdS-P}$

$\text{BiVO}_4/\text{Au}@\text{CdS-P}$  is synthesized using the same method as synthesis of  $\text{BiVO}_4/\text{Au}@\text{CdS}$  samples, but instead of  $\text{BiVO}_4$  by  $\text{BiVO}_4$ -P.

## 2.2. Material characterization

The crystal structures of the as-prepared samples are identified by X-ray diffraction (XRD). XRD patterns are carried out on a Bruker D8 ADVANCE X-ray diffractometer with  $\text{Cu K}\alpha$  radiation ( $\lambda = 0.15418 \text{ nm}$ ), which operated at 40 kV and 40 mA. The scan rate is 0.5 ( $20 \text{ s}^{-1}$ ). Scanning electron microscopy (SEM) images are obtained using a HITACHI SU8000 field-emission scanning electron microscope, equipped with energy-dispersive X-ray spectroscopy (EDX) for elemental analysis. X-ray photoelectron spectroscopy (XPS) investigation is recorded on a Thermo Scientific ESCA Lab 250 system with a monochromatic  $\text{Al K}\alpha$  as the X-ray source and hemispherical analyzer. And sample stage with multi-axial adjustability and the surface composition are analyzed by XPS. UV-vis diffuse reflectance spectroscopy (DRS) is measured by a Carry 500 UV-vis spectrophotometer, during which  $\text{BaSO}_4$  is served as the background. The photoelectrochemical measurement is similar to previous report [21]. The BAS Epsilon workstation is utilized to monitor the photocurrents of samples. The working electrode is prepared on fluoride tin oxide (FTO) conductor glass. Typically, 10 mg sample powder is mixed with 1 mL DMF to make slurry. The slurry is then spread onto the FTO glass, whose side part is previously protected using 95 Scotch tapes. The working electrode is further dried at 100 °C for 3 h to improve adhesion. A 300W Xe lamp equipped with a 420 nm cut-off filter is used as visible light source. 0.2 M of aqueous  $\text{Na}_2\text{SO}_4$  solution is used as the supporting electrolyte. Total organic carbon (TOC) assays of the degraded solution after 6 h of irradiation are carried out on a TOC analyzer (TOC-VCPh, Shimadzu).

## 2.3. Photocatalytic activity measurement

The photo-degradation of RhB in aqueous solution is done in a Pyrex glass vessel. Typically, 30 mg of the photocatalyst is dispersed into 50 mL of RhB aqueous solution ( $5 \text{ mg L}^{-1}$ ) in the Pyrex glass vessel. Before illumination, all suspensions are kept in the dark for 30 min with stirring to ensure the adsorption–desorption equilibrium had been established. Then the suspension is illuminated under a 300 W Xe lamp with a 420 nm band-pass filter. And the photo-degradation came into operation. During the process of photodegradation, the concentrations of RhB in the suspension, collected at interval 20 min, is detected respectively by a Cary-500 UV-vis spectrophotometer. The normalized concentration changes ( $C/C_0$ ) of RhB solution during the photo-degradation are proportional to the normalized maximum absorbance ( $A/A_0$ ) and derived from the changes in the dye's absorption profile (554 nm for RhB) at a given time interval.

## 3. Results and discussions

### 3.1. Phase structure and morphology

Samples at different stages ( $\text{BiVO}_4$ ,  $\text{BiVO}_4/\text{Au}$ ,  $\text{BiVO}_4/\text{Au}@\text{CdS}$  and  $\text{BiVO}_4/\text{Au}@\text{CdS-P}$ ) are characterized by powder X-ray diffraction (XRD) to analyze their crystallographic structure and phase purity (Fig. 2). The diffraction peaks for all samples match well with the pure monoclinic phase of  $\text{BiVO}_4$  corresponding to the JCPDS No. 75-1866, indicating that the introduction of Au and CdS does not change the crystal phase and crystallinity of  $\text{BiVO}_4$ , which may be attributed to the low content of Au and CdS [37,38]. More evidences of existing Au and CdS have been given in other characters.

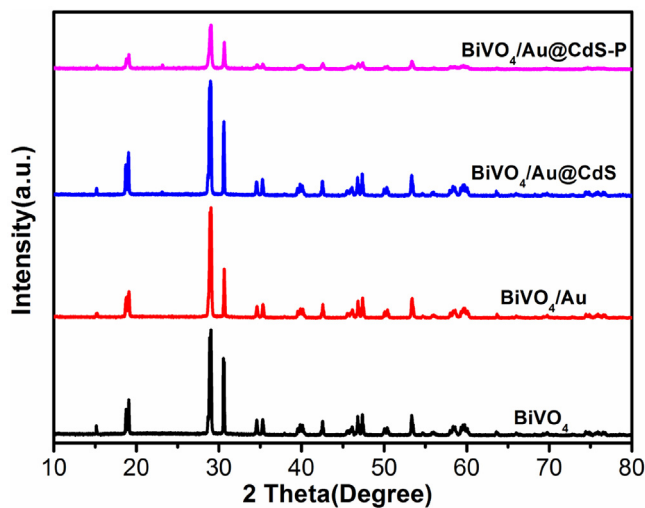


**Fig. 2.** XRD patterns of the  $\text{BiVO}_4$ ,  $\text{BiVO}_4/\text{Au}$ ,  $\text{BiVO}_4/\text{Au@CdS}$  and  $\text{BiVO}_4/\text{Au@CdS-P}$ .

As shown in Fig. 3, the morphological structure of  $\text{BiVO}_4$ ,  $\text{BiVO}_4/\text{Au}$ ,  $\text{BiVO}_4/\text{Au@CdS}$  and  $\text{BiVO}_4/\text{Au@CdS-P}$  photocatalysts are characterized by scanning electron microscopy (SEM). In Fig. 3a, the pure  $\text{BiVO}_4$  composed mainly of  $\{010\}$  and  $\{110\}$  facet is obtained successfully by a hydrothermal method. The photogenerated elec-

trons and holes tend to accumulate on the  $\{010\}$  and  $\{110\}$  facets, respectively, due to these facets have different energy levels in the conduction bands and the valence bands [28]. Based on this principle, Au particles will be photoreduced on the  $\{010\}$  facets of  $\text{BiVO}_4$  crystals. Fig. 3b shows the SEM image of  $\text{BiVO}_4/\text{Au}$ . As shown in Fig. 3b, Au particles distribute only on the  $\{010\}$  facets of  $\text{BiVO}_4$  crystals and no aggregation occurs for Au nanoparticles. This will be further proved by other characters, including SEM-EDX and DRS. SEM image of  $\text{BiVO}_4/\text{Au@CdS}$  is shown in Fig. 3c. CdS nanoparticles are deposited onto the surfaces of the Au nanoparticles by photodeposition. The further evidences of  $\text{Au@CdS}$  are given by other characters, including SEM-EDX and diameter distribution. The SEM-EDX image and corresponding description can be seen in Fig.S1. As shown in Fig. 3d,  $\text{BiVO}_4/\text{Au@CdS-P}$  sample without  $\{010\}$  and  $\{110\}$  facets exposed is smaller than those of  $\text{BiVO}_4/\text{Au@CdS}$ , and the size of particles is nonuniform. This is agreement with BET characterization as shown in Table S1.

The diameter distribution of the Au nanoparticles is estimated from the SEM image in Fig. 4a, indicating that the mean diameter of Au nanoparticles is about 21.43 nm. While Fig. 4b shows the diameter distribution of the  $\text{Au@CdS}$  nanoparticles, indicating that the mean diameter of  $\text{Au@CdS}$  nanoparticles is about 34.71 nm. This result can indirectly justify that CdS nanoparticles can be deposited onto the surfaces of the Au nanoparticles by photodeposition.

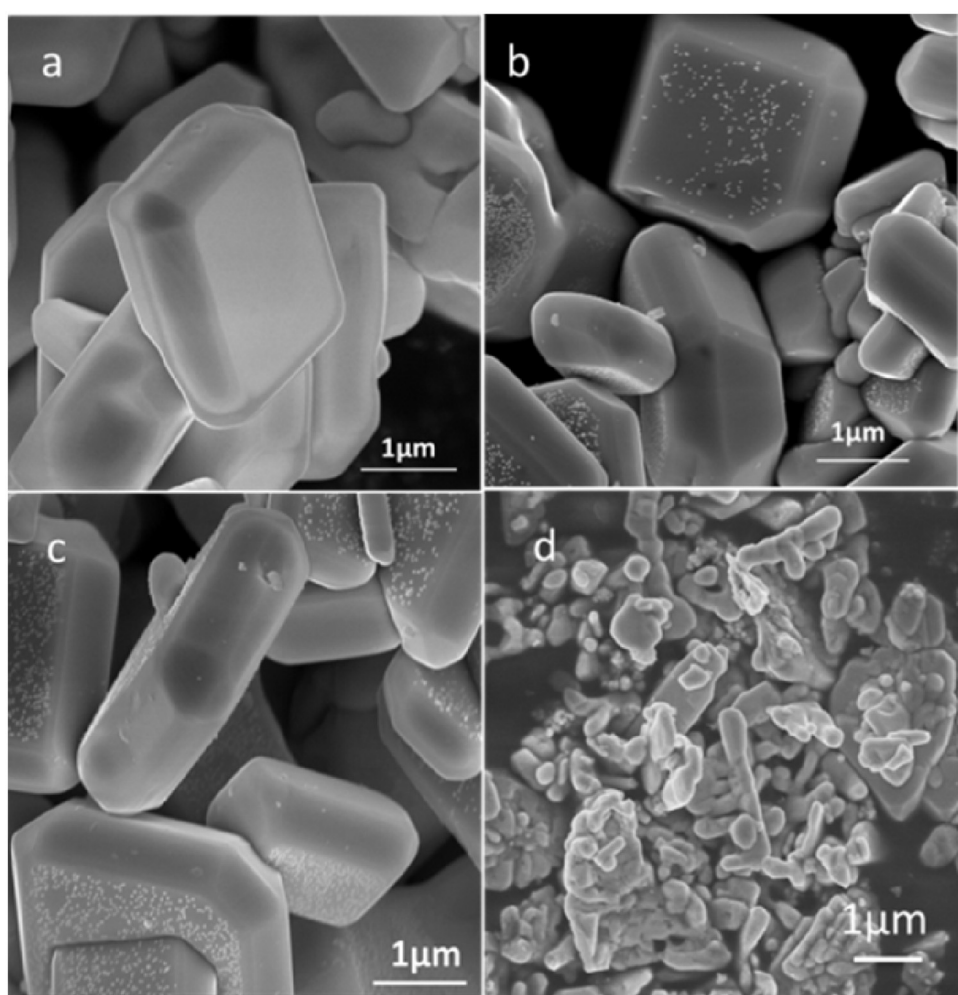


**Fig. 3.** SEM images of the (a)  $\text{BiVO}_4$ , (b)  $\text{BiVO}_4/\text{Au}$ , (c)  $\text{BiVO}_4/\text{Au@CdS}$  and (d)  $\text{BiVO}_4/\text{Au@CdS-P}$ .

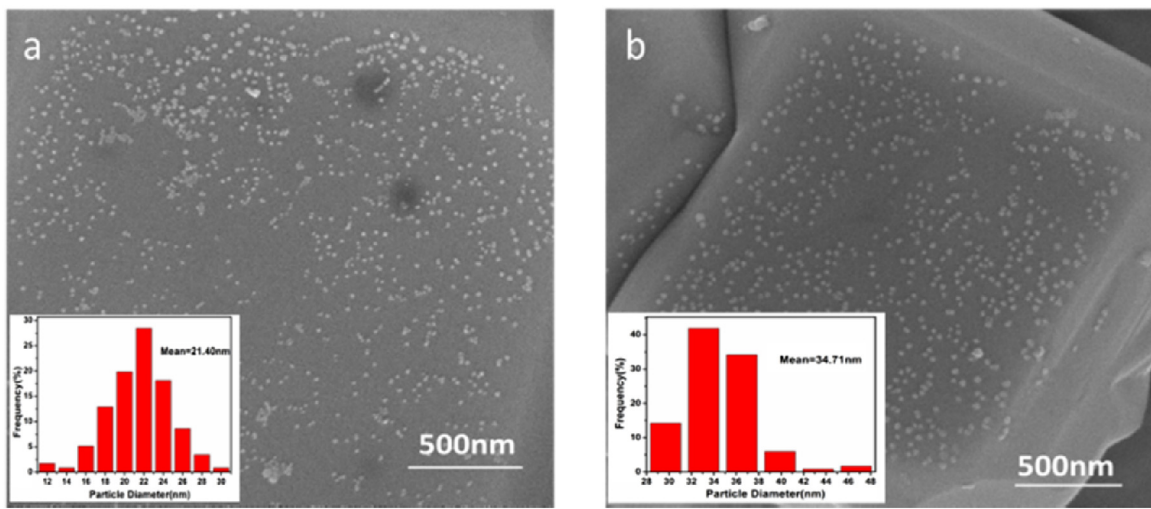


Fig. 4. SEM image with statistics (inset) of (a) BiVO<sub>4</sub>/Au, (b) BiVO<sub>4</sub>/Au@CdS.

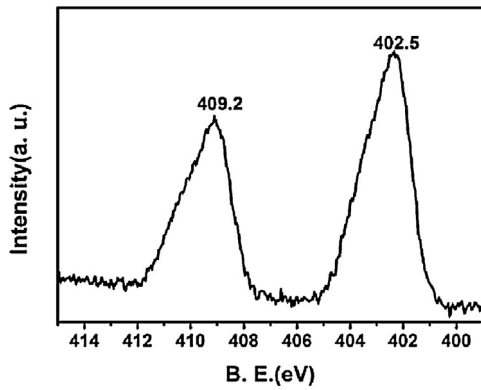


Fig. 5. XPS spectra of Cd 3d peaks of BiVO<sub>4</sub>/Au@CdS.

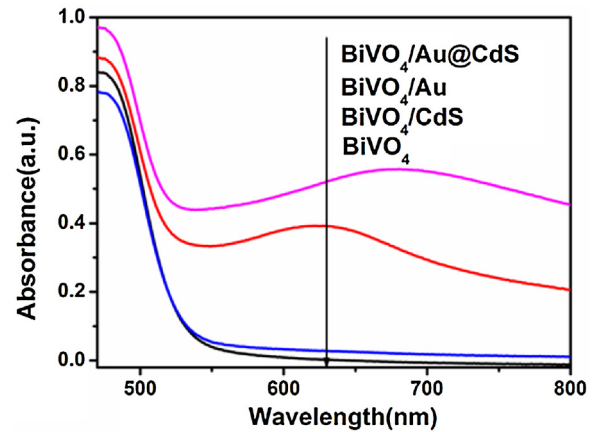


Fig. 6. UV-vis diffuse reflectance spectrum of BiVO<sub>4</sub>, BiVO<sub>4</sub>/Au, BiVO<sub>4</sub>/CdS and BiVO<sub>4</sub>/Au@CdS.

### 3.2. Chemical composition

More evidences of existence of Au@CdS on the BiVO<sub>4</sub> can be further proved by analyzing the XPS characterization. As displayed in Fig. 5, the Cd 3d<sub>5/2</sub> and Cd 3d<sub>3/2</sub> peaks located at 402.5 and 409.2 eV with a spin-orbit separation of 6.7 eV are consistent with the reported values for Cd<sup>2+</sup> states in CdS [14]. Owing to the peaks of S are closed to peaks of Bi, as well as the low content of CdS, the peaks of S are covered with peaks of Bi. So Cd can be measured to reflect the existence of CdS.

The Au nanoparticles by the photodeposition in low concentration are too small to detect by energy dispersion spectrometry. In order to reflect that CdS nanoparticles can be deposited on the surfaces of the Au nanoparticles by photo-deposition, 10-fold concentration of HAuCl<sub>4</sub> is used in the preparation to obtain large-sized Au nanoparticles. As shown in Fig. S1a in Supplementary material, the SEM-EDX image of BiVO<sub>4</sub>/Au can be obviously observed that Au nanoparticles deposit on the {010} facets of BiVO<sub>4</sub>. As shown in Fig. S1b in Supplementary material, it is found that Cd and S can be detected on Au nanoparticles by EDX in BiVO<sub>4</sub>/Au@CdS. However, in other area, no Cd and S can be detected. Combined with diameter distribution analysis and XPS characterization of Cd, it can conclude that CdS nanoparticles deposit onto the surfaces of the Au nanoparticles.

### 3.3. Optical properties

UV-vis diffuse reflectance spectroscopy (DRS) is employed to examine their optical properties in Fig. 6. The existence of CdS extends the optical absorption limit from 535 nm to 550 nm. While adopting Au nanoparticles upon BiVO<sub>4</sub>, a noticeable broad shoulder peak centers at 615 nm, corresponding to the plasmonic absorption of Au nanoparticles and indicating the existence of Au nanoparticles and CdS [39]. Compared to BiVO<sub>4</sub>, BiVO<sub>4</sub>/Au and BiVO<sub>4</sub>/CdS, BiVO<sub>4</sub>/Au@CdS composites show a broader absorption in visible light region and increase absorption intensity [40], which indicates intimate contact between Au and CdS [39,41]. This composite can absorb and utilize visible light more efficiently, leading to the higher photocatalytic activities [42].

### 3.4. Photocatalytic activity

As a typical pollutant model for evaluation of the photocatalytic performance, an organic dye, Rhodamine B (RhB) is employed to study the photocatalytic activities of samples under visible light irradiation as shown in Fig. 7a, which displays photodegradation dynamic curves over aforementioned photocatalysts. Compared with the pristine BiVO<sub>4</sub>, BiVO<sub>4</sub>/Au, BiVO<sub>4</sub>/CdS and BiVO<sub>4</sub>/CdS/Au, BiVO<sub>4</sub>/Au@CdS exhibits a prodigious progress in degradation of RhB solution under visible light irradiation. Owing to the low

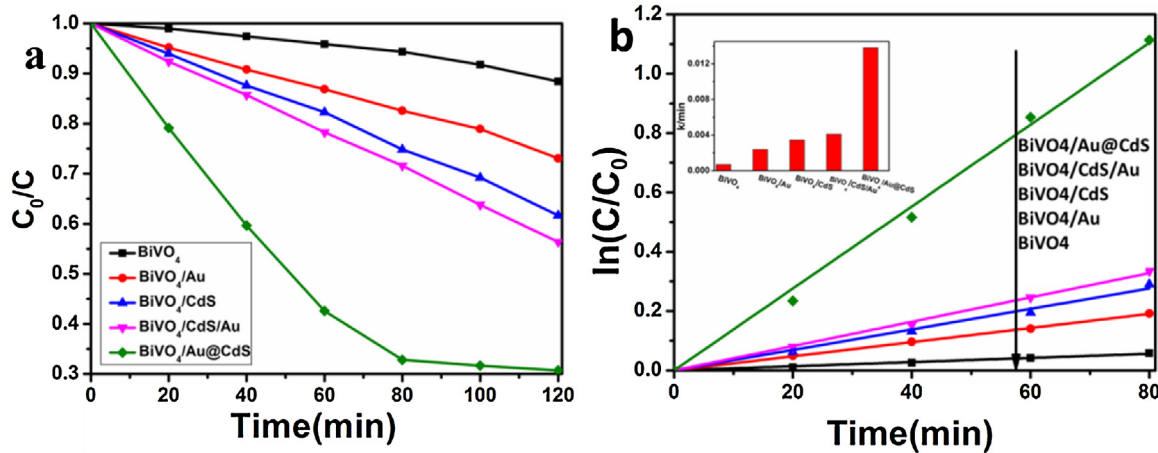


**Fig. 7.** (a) Comparison of photocatalytic performance of the prepared samples on the degradation of RhB dye under visible light irradiation; (b) Kinetics of RhB degradation reaction over the samples.

concentration of the RhB solution ( $5\text{ mg L}^{-1}$ ), the kinetics of the photocatalytic reactions are followed as a pseudo first order reaction, which can be expressed as:  $\ln(C_0/C_t) = k_{\text{app}}t$  [16]. Here  $C_t$  is the concentration of RhB at irradiation time  $t$ ,  $C_0$  is the initial concentration of RhB. Then,  $k_{\text{app}}$  is the apparent reaction rate constant, which can be obtained from the slope of the liner correlation. As shown in Fig. 7b, apparently, such Z-scheme  $\text{BiVO}_4/\text{Au}@\text{CdS}$  photocatalyst presents the highest  $k_{\text{app}}$  value of  $0.0138\text{ min}^{-1}$ , which is about 3.4, 4.0, 5.8 and 19.7 times as that of  $\text{BiVO}_4/\text{CdS}/\text{Au}$  ( $k_{\text{app}} = 0.0041\text{ min}^{-1}$ ),  $\text{BiVO}_4/\text{CdS}$  ( $k_{\text{app}} = 0.00345\text{ min}^{-1}$ ),  $\text{BiVO}_4/\text{Au}$  ( $k_{\text{app}} = 0.00238\text{ min}^{-1}$ ) and  $\text{BiVO}_4$  ( $k_{\text{app}} = 0.0007\text{ min}^{-1}$ ), respectively. These results further confirms that the  $\text{BiVO}_4/\text{Au}@\text{CdS}$  keeps the highest charge carrier separation efficiency, which is also supported by the results from the photocurrent density.

As a comparison, photocatalytic performance of samples after normalized treatment by using the specific surface area is shown in Table S1. Although  $\text{BiVO}_4/\text{Au}@\text{CdS-P}$  has higher surface area than  $\text{BiVO}_4/\text{Au}@\text{CdS}$ ,  $k_{\text{app}}$  of  $\text{BiVO}_4/\text{Au}@\text{CdS}$  is about 36 times as that of  $\text{BiVO}_4/\text{Au}@\text{CdS-P}$  after normalization. As shown in Fig. S2, before normalized treatment, the photocatalytic performance of  $\text{BiVO}_4/\text{Au}@\text{CdS}$  is obviously higher than that of  $\text{BiVO}_4/\text{Au}@\text{CdS-P}$ . Furthermore, the extent of mineralization is evaluated by measuring the total organic carbon (TOC) in Fig. S3 in Supplementary material. After irradiation for 6 h, the TOC value of the final solution for  $\text{BiVO}_4/\text{Au}@\text{CdS}$  is  $1.88\text{ mg L}^{-1}$ , while it is  $3.35\text{ mg L}^{-1}$  for  $\text{BiVO}_4/\text{Au}@\text{CdS-P}$ . The corresponding mineralization efficiency is evaluated to be ca. 76% for  $\text{BiVO}_4/\text{Au}@\text{CdS}$  and 57% for  $\text{BiVO}_4/\text{Au}@\text{CdS-P}$ . According to the above comparison and analysis, it can be concluded that construction of Z-scheme photocatalytic system is the main factor to enhance photocatalytic performance.

To further understand the effect of Z-scheme photocatalytic system on the separation efficiency of photogenerated electron-hole pairs, the transient photocurrent responses of  $\text{BiVO}_4$ ,  $\text{BiVO}_4/\text{Au}$ ,  $\text{BiVO}_4/\text{CdS}/\text{Au}$ ,  $\text{BiVO}_4/\text{Au}@\text{CdS-P}$  and  $\text{BiVO}_4/\text{Au}@\text{CdS}$  are recorded for several on-off cycles under visible light irradiation as shown in Fig. 8. Notably, the  $\text{BiVO}_4/\text{Au}@\text{CdS}$  Z-scheme photocatalytic system shows the highest photocurrent density in the all  $\text{BiVO}_4$ -based samples, indicating the increase of charge carriers transferred from  $\text{BiVO}_4/\text{Au}@\text{CdS}$  composite to the working electrode surface [14,43]. This result has agreement with photocatalytic performance. Besides, there are two notable observations in the transient photocurrent responses of  $\text{BiVO}_4/\text{Au}@\text{CdS-P}$ . The photocurrent quickly decays to about 30% level to provide stable photocurrent. This initial decay shows the limitation of sustaining efficient

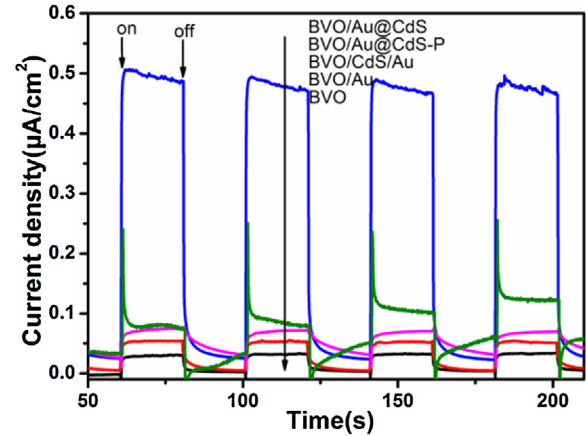


**Fig. 8.** Transient photocurrent responses of the samples in  $0.2\text{ M Na}_2\text{SO}_4$  with  $0.2\text{ V}$  bias potential versus  $\text{Ag}/\text{AgCl}$  electrodes at visible light illumination.

transport of photogenerated electrons to the FTO electrode surface arising from recombination losses [44,45], which indicates  $\text{BiVO}_4/\text{Au}@\text{CdS-P}$  has more serious photogenerated charge carriers recombination than  $\text{BiVO}_4/\text{Au}@\text{CdS}$ . With the above analysis, it can be concluded that introducing facet engineering into Z-scheme photocatalytic system provide an efficient separation channel, which can reduce the recombination of charge carriers. Another interesting observation in the photocurrent response is a reversal of the photocurrent when the light is turned off, which indicating that the cathodic (or reverse) current competes with the anodic photocurrent during the illumination of the  $\text{BiVO}_4/\text{Au}@\text{CdS-P}$  electrode. This behavior has been noted in a few earlier studies [46] and is a result of recombination of electrons with oxidized forms of the redox couple at the electrode–electrolyte interface [46].

### 3.5. Photocatalytic mechanism

A tentative mechanism for the photochemical processes is depicted in Scheme 1. Under the visible light illumination, both  $\text{BiVO}_4$  and  $\text{CdS}$  can be excited at the same time. For  $\text{BiVO}_4$  photocatalyst, the photogenerated electrons and holes tend to accumulate on the  $\{010\}$  and  $\{110\}$  facets, respectively, which decreases the bulk recombination of charge carriers, leading to more electrons transfer to conduction band (CB) of  $\text{BiVO}_4$  photocatalyst. Then there more electrons can recombine with more holes located at the valence band (VB) of  $\text{CdS}$  through gold particles conductor.

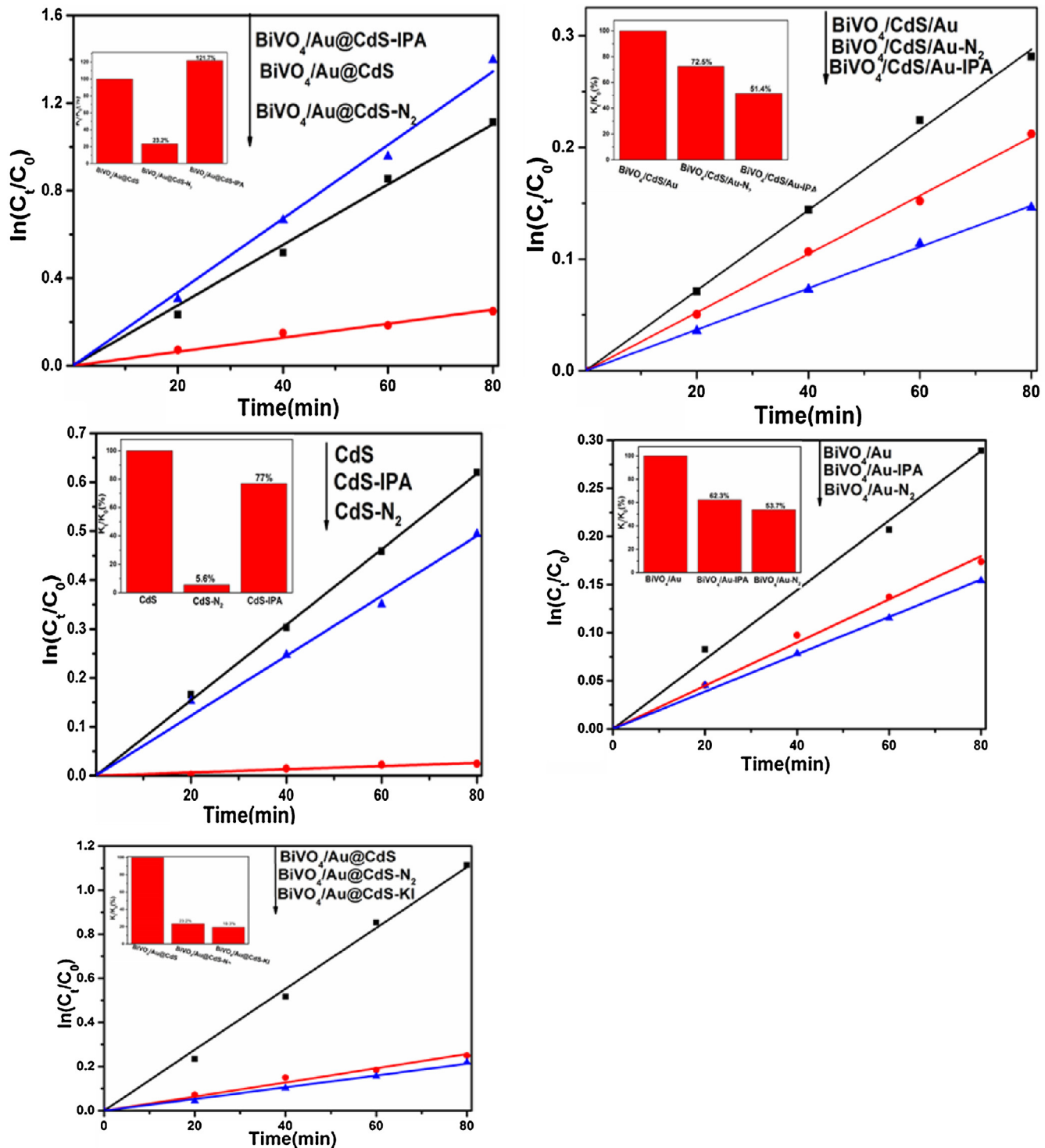
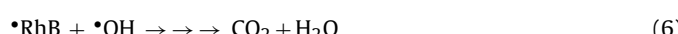
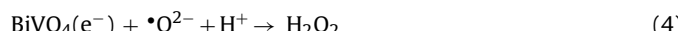
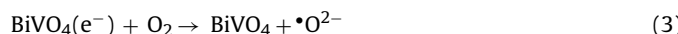
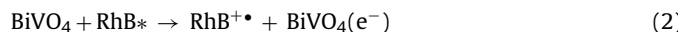


Fig. 9. Trapping experiment of the active species during the photocatalytic reaction.

Thus itself recombination can be indirectly decreased in CdS and  $\text{BiVO}_4$  respectively. Owing to more holes of CdS are recombined with electrons of  $\text{BiVO}_4$ , there will be more electrons of CdS stay on the conduction band (CB) of CdS. In this case, the electrons with higher reducibility on conduction band (CB) of CdS and the holes with higher oxidizability on valence band (VB) of  $\text{BiVO}_4$  can participate in photodegradation process, leading high photocatalytic performance. More electrons in CdS can react with surface adsorbed oxygen molecules to form  $\cdot\text{O}_2^-$ , which pro-

mote the degradation of RhB. Meanwhile, more holes in  $\text{BiVO}_4$  can also directly participate in reaction to promote the degradation of RhB. Thus, facet-depended all-solid-state visible Z-scheme photocatalytic system of  $\text{BiVO}_4/\text{Au}@\text{CdS}$  has higher photocatalytic performance. Therein, Au nanoparticles dominantly play the role of electron mediator for extracting electrons from  $\text{BiVO}_4$  and pouring electrons into CdS. The detail discussion is presented in Supporting Information.

In order to further validate the high photocatalytic activity mechanism of the Z-scheme photocatalytic system of  $\text{BiVO}_4/\text{Au}@\text{CdS}$ , the reactive species trapping experiments have been performed as shown in Fig. 9. The concentration of all scavengers is 0.01 M in the following experiments. The KI is  $\text{h}^+$  scavenger, bubbling  $\text{N}_2$  captures  $\cdot\text{O}_2^-$  radical and IPA is  $\cdot\text{OH}$  radical scavenger. The explanation is mainly focused on the electrons, while the hole is used as an auxiliary.  $\text{BiVO}_4/\text{CdS}/\text{Au}$  is prepared in order to compare with  $\text{BiVO}_4/\text{Au}@\text{CdS}$  with Z-scheme photocatalytic system. The photocatalytic mechanism of  $\text{BiVO}_4/\text{CdS}/\text{Au}$  is a typical heterostructure photocatalytic mechanism. Electrons on conduction band (CB) of  $\text{BiVO}_4$  and holes on valence band (VB) of  $\text{CdS}$  can participate in photodegradation process. As shown in Fig. 9a and 9e, it can be clearly seen that bubbling  $\text{N}_2$  and KI cause fast deactivation of the  $\text{BiVO}_4/\text{Au}@\text{CdS}$ , which demonstrates that  $\cdot\text{O}_2^-$  and  $\text{h}^+$  are the predominant active species. It can assume that the electrons in  $\text{CdS}$  preferentially react with surface adsorbed oxygen molecules to form  $\cdot\text{O}_2^-$ . As shown in Fig. 9b, IPA retards reaction rate of the  $\text{BiVO}_4/\text{CdS}/\text{Au}$ , which demonstrates that  $\cdot\text{OH}$  is the predominant active species. It can assume that electrons in  $\text{BiVO}_4$  preferentially form  $\cdot\text{OH}$ . In order to prove aforementioned assumptions, the reactive species trapping experiments of  $\text{BiVO}_4/\text{Au}$  and  $\text{CdS}$  have been performed. As shown in Fig. 9c, bubbling  $\text{N}_2$  caused fast deactivation of the  $\text{C}/\text{C}_0$  ( $\text{CdS}$ ), which demonstrates that  $\cdot\text{O}_2^-$  is the predominant active species. This result has agreement with aforementioned assumptions. Besides, as shown in Fig. 9d, both bubbling  $\text{N}_2$  and IPA can retard reaction rate of the  $\text{BiVO}_4/\text{Au}$ , and their results are similar. According to following equations, it shows that  $\cdot\text{O}_2^-$  can be converted into  $\cdot\text{OH}$  [47].



Therefore, both bubbling  $\text{N}_2$  and IPA can be thought as an indirect scavenger for  $\cdot\text{OH}$  radical. This result also has agreement with aforementioned assumptions. Under the premise above, some phenomena can be explained. As shown in Fig. 9a, introducing IPA can slightly promote reaction rate of the  $\text{BiVO}_4/\text{Au}@\text{CdS}$ . It can be explained in the following. Owing to the electrons in  $\text{BiVO}_4$  preferentially to form  $\cdot\text{OH}$ , introducing IPA can indirectly consume the electrons in  $\text{BiVO}_4$ , leading more holes in  $\text{BiVO}_4$  remain down, which can promote photocatalytic performance because  $\text{h}^+$  is also the predominant active species.

#### 4. Conclusions

In summary, all-solid-state visible Z-scheme photocatalytic system of  $\text{BiVO}_4/\text{Au}@\text{CdS}$  is successfully synthesized, which is selectively built on the  $\{010\}$  facet of  $\text{BiVO}_4$  crystals in this system. This work aims at construction of dual-channel by realizing complementarity of interfacial engineering and facet engineering, for promoting effective separation of charge carriers and optimizing transfer channel of electrons in Z-scheme photocatalytic system. Such vectorial migration of photogenerated charge carriers through multiple order transmission channels in Z-scheme photocatalytic system realizes effective separation of photogenerated charge carriers and high performance. Our current work is expected to offer new insight into construction of multiple order transmission channels for rational design and synthesis of photocatalyst with high performance.

#### Acknowledgements

This work is supported by the National Natural Science Foundation of China (21473031, 21273035, 21673041 and 21173046), the National Basic Research Program of China (973 Program: 2013CB632405), the National Key Technologies R & D Program of China (2014BAC13B03) and the Science & Technology Plan Project of Fujian Province (2014Y2003).

#### Appendix A. Supplementary data

Supplementary data associated with this article can be found, in the online version, at <http://dx.doi.org/10.1016/j.apcatb.2017.04.049>.

#### References

- [1] H. Park, H.-i Kim, G.-h Moon, W. Choi, Photoinduced charge transfer processes in solar photocatalysis based on modified  $\text{TiO}_2$ , *Energy Environ. Sci.* (2016).
- [2] Y. Ma, X. Wang, Y. Jia, X. Chen, H. Han, C. Li, Titanium dioxide-based nanomaterials for photocatalytic fuel generations, *Chem. Rev.* 114 (2014) 9987–10043.
- [3] S. Yu, Y.H. Kim, S.Y. Lee, H.D. Song, J. Yi, Hot-electron-transfer enhancement for the efficient energy conversion of visible light, *Angew. Chem.* 53 (2014) 11203–11207.
- [4] L. Mu, Y. Zhao, A. Li, S. Wang, Z. Wang, J. Yang, Y. Wang, T. Liu, R. Chen, J. Zhu, F. Fan, R. Li, C. Li, Enhancing charge separation on high symmetry  $\text{SrTiO}_3$  exposed with anisotropic facets for photocatalytic water splitting, *Energy Environ. Sci.* (2016).
- [5] J. Yu, M. Jaroniec, Energy and environmental photocatalytic materials, *Appl. Surf. Sci.* 391 (2017) 71.
- [6] H. Tada, M. Fujishima, H. Kobayashi, Photodeposition of metal sulfide quantum dots on titanium(IV) dioxide and the applications to solar energy conversion, *Chem. Soc. Rev.* 40 (2011) 4232–4243.
- [7] L. Shi, K. Chang, H. Zhang, X. Hai, L. Yang, T. Wang, J. Ye, Drastic enhancement of photocatalytic activities over phosphoric acid protonated porous  $\text{g-C}_3\text{N}_4$  nanosheets under visible light, *Small* 12 (2016) 4431–4439.
- [8] Y. Kang, Y. Yang, L.C. Yin, X. Kang, L. Wang, G. Liu, H.M. Cheng, Selective breaking of hydrogen bonds of layered carbon nitride for visible light photocatalysis, *Adv. Mater.* (2016).
- [9] Y. Sasaki, H. Kato, A. Kudo,  $[\text{Co}(\text{bpy})_3](3+/2+)$  and  $[\text{Co}(\text{phen})_3](3+/2+)$  electron mediators for overall water splitting under sunlight irradiation using Z-scheme photocatalyst system, *J. Am. Chem. Soc.* 135 (2013) 5441–5449.
- [10] M.-V. Sofianou, M. Tassi, V. Pscharis, N. Boukos, S. Thanos, T. Vaimakis, J. Yu, C. Trapalis, Solvothermal synthesis and photocatalytic performance of  $\text{Mn}^{4+}$ -doped anatase nanoplates with exposed  $\{001\}$  facets, *Appl. Catal. B: Environ.* 162 (2015) 27–33.
- [11] S. Guo, Y. Zhu, Y. Yan, Y. Min, J. Fan, Q. Xu, Holey structured graphitic carbon nitride thin sheets with edge oxygen doping via photo-Fenton reaction with enhanced photocatalytic activity, *Appl. Catal. B: Environ.* 185 (2016) 315–321.
- [12] X. Ji, Z. Su, P. Wang, G. Ma, S. Zhang, Integration of artificial photosynthesis system for enhanced electronic energy-transfer efficacy: a case study for solar-energy driven bioconversion of carbon dioxide to methanol, *Small* 12 (2016) 4753–4762.
- [13] Y. Kim, D. Shin, W.J. Chang, H.L. Jang, C.W. Lee, H.-E. Lee, K.T. Nam, Hybrid Z-scheme using photosystem I and  $\text{BiVO}_4$  for hydrogen production, *Adv. Funct. Mater.* 25 (2015) 2369–2377.
- [14] J. Jin, J. Yu, D. Guo, C. Cui, W. Ho, A hierarchical Z-Scheme  $\text{cdS-WO}_3$  photocatalyst with enhanced  $\text{CO}_2$  reduction activity, *Small* 11 (2015) 5262–5271.
- [15] J. Yan, H. Wu, H. Chen, Y. Zhang, F. Zhang, S.F. Liu, Fabrication of  $\text{TiO}_2/\text{C}_3\text{N}_4$  heterostructure for enhanced photocatalytic Z-scheme overall water splitting, *Appl. Catal. B: Environ.* 191 (2016) 130–137.
- [16] H. Li, Y. Sun, B. Cai, S. Gan, D. Han, L. Niu, T. Wu, Hierarchically Z-scheme photocatalyst of  $\text{Ag}/\text{AgCl}$  decorated on  $\text{BiVO}_4$  (040) with enhancing photoelectrochemical and photocatalytic performance, *Appl. Catal. B: Environ.* 170–171 (2015) 206–214.
- [17] B. Zhu, P. Xia, Y. Li, W. Ho, J. Yu, Fabrication and photocatalytic activity enhanced mechanism of direct Z-scheme  $\text{g-C}_3\text{N}_4/\text{Ag}_2\text{WO}_4$  photocatalyst, *Appl. Surf. Sci.* 391 (2017) 175–183.
- [18] D. Zheng, C. Pang, X. Wang, The function-led design of Z-scheme photocatalytic systems based on hollow carbon nitride semiconductors, *Chem. Commun.* 51 (2015) 17467–17470.
- [19] P. Zhou, J. Yu, M. Jaroniec, All-solid-state Z-scheme photocatalytic systems, *Adv. Mater.* 26 (2014) 4920–4935.
- [20] C. Li, P. Zhang, R. Lv, J. Lu, T. Wang, S. Wang, H. Wang, J. Gong, Selective deposition of  $\text{Ag}_3\text{PO}_4$  on monoclinic  $\text{BiVO}_4$ (040) for highly efficient photocatalysis, *Small* 9 (2013) 3951–3956.
- [21] Z. Fang, S. Weng, X. Ye, W. Feng, Z. Zheng, M. Lu, S. Lin, X. Fu, P. Liu, Defect engineering and phase junction architecture of wide-bandgap  $\text{ZnS}$  for

conflicting visible light activity in photocatalytic H<sub>2</sub> evolution, *ACS Appl. Mater. Interfaces* 7 (2015) 13915–13924.

[22] X.L. Yin, J. Liu, W.J. Jiang, X. Zhang, J.S. Hu, L.J. Wan, Urchin-like Au@Cds/WO<sub>3</sub> micro/nano heterostructure as a visible-light driven photocatalyst for efficient hydrogen generation, *Chem. Commun.* 51 (2015) 13842–13845.

[23] Z.B. Yu, Y.P. Xie, G. Liu, G.Q. Lu, X.L. Ma, H.-M. Cheng, Self-assembled CdS/Au/ZnO heterostructure induced by surface polar charges for efficient photocatalytic hydrogen evolution, *J. Mater. Chem. A* 1 (2013) 2773.

[24] F. Chen, Q. Yang, X. Li, G. Zeng, D. Wang, C. Niu, J. Zhao, H. An, T. Xie, Y. Deng, Hierarchical assembly of graphene-bridged Ag<sub>3</sub>PO<sub>4</sub>/Ag/BiVO<sub>4</sub> (040) Z-scheme photocatalyst: an efficient, sustainable and heterogeneous catalyst with enhanced visible-light photoactivity towards tetracycline degradation under visible light irradiation, *Appl. Catal. B: Environ.* 200 (2017) 330–342.

[25] Y. Min, G. He, Q. Xu, Y. Chen, Self-assembled encapsulation of graphene oxide/Ag@AgCl as a Z-scheme photocatalytic system for pollutant removal, *J. Mater. Chem. A* 2 (2014) 1294–1301.

[26] A. Iwase, Y.H. Ng, Y. Ishiguro, A. Kudo, R. Amal, Reduced graphene oxide as a solid-state electron mediator in Z-scheme photocatalytic water splitting under visible light, *J. Am. Chem. Soc.* 133 (2011) 11054–11057.

[27] A. Meng, J. Zhang, D. Xu, B. Cheng, J. Yu, Enhanced photocatalytic H<sub>2</sub>-production activity of anatase TiO<sub>2</sub> nanosheet by selectively depositing dual-cocatalysts on {101} and {001} facets, *Appl. Catal. B: Environ.* 198 (2016) 286–294.

[28] R. Li, F. Zhang, D. Wang, J. Yang, M. Li, J. Zhu, X. Zhou, H. Han, C. Li, Spatial separation of photogenerated electrons and holes among {010} and {110} crystal facets of BiVO<sub>4</sub>, *Nat. Commun.* 4 (2013) 1432.

[29] H. Li, H. Yu, X. Quan, S. Chen, H. Zhao, Improved photocatalytic performance of heterojunction by controlling the contact facet: high electron transfer capacity between TiO<sub>2</sub> and the {110} facet of BiVO<sub>4</sub> caused by suitable energy band alignment, *Adv. Funct. Mater.* 25 (2015) 3074–3080.

[30] W. Feng, S. Weng, Z. Zheng, Z. Fang, P. Liu, <sup>1</sup>Rational design of a charge shunt: modification upon crystal facet engineering of semiconductor photocatalysts, *Chem. Commun.* 51 (2015) 11186–11189.

[31] M. Huang, S. Weng, B. Wang, J. Hu, X. Fu, P. Liu, Various facet tunable ZnO crystals by a scalable solvothermal synthesis and their facet-dependent photocatalytic activities, *J. Phys. Chem. C* 118 (2014) 25434–25440.

[32] N. Zhang, C. Chen, Z. Mei, X. Liu, X. Qu, Y. Li, S. Li, W. Qi, Y. Zhang, J. Ye, V.A. Roy, R. Ma, Monoclinic tungsten oxide with {100} facet orientation and tuned electronic band structure for enhanced photocatalytic oxidations, *ACS Appl. Mater. Interfaces* 8 (2016) 10367–10374.

[33] L. Ye, X. Jin, X. Ji, C. Liu, Y. Su, H. Xie, C. Liu, Facet-dependent photocatalytic reduction of CO<sub>2</sub> on BiOI nanosheets, *Chem. Eng. J.* 291 (2016) 39–46.

[34] L. Li, B. Yan, BiVO<sub>4</sub>/Bi<sub>2</sub>O<sub>3</sub> submicrometer sphere composite: microstructure and photocatalytic activity under visible-light irradiation, *J. Alloys Compd.* 476 (2009) 624–628.

[35] F.Q. Zhou, J.C. Fan, Q.J. Xu, Y.L. Min, BiVO<sub>4</sub> nanowires decorated with CdS nanoparticles as Z-scheme photocatalyst with enhanced H<sub>2</sub> generation, *Appl. Catal. B: Environ.* 201 (2017) 77–83.

[36] H. Tada, T. Mitsui, T. Kiyonaga, T. Akita, K. Tanaka, All-solid-state Z-scheme in CdS-Au-TiO<sub>2</sub> three-component nanojunction system, *Nat. Mater.* 5 (2006) 782–786.

[37] Y. Liu, P. Zhang, B. Tian, J. Zhang, Core–shell structural CdS@SnO<sub>2</sub> nanorods with excellent visible-light photocatalytic activity for the selective oxidation of benzyl alcohol to benzaldehyde, *ACS Appl. Mater. Interfaces* 7 (2015) 13849–13858.

[38] D. Lang, F. Cheng, Q. Xiang, Enhancement of photocatalytic H<sub>2</sub>-production activity of CdS nanorods by cobalt-based cocatalysts modification, *Catal. Sci. Technol.* (2016).

[39] J. Li, S.K. Cushing, P. Zheng, T. Senty, F. Meng, A.D. Bristow, A. Manivannan, N. Wu, Solar hydrogen generation by a CdS-Au-TiO<sub>2</sub> sandwich nanorod array enhanced with Au nanoparticle as electron relay and plasmonic photosensitizer, *J. Am. Chem. Soc.* 136 (2014) 8438–8449.

[40] Y. Min, G. He, Q. Xu, Y. Chen, Dual-functional MoS<sub>2</sub> sheet-modified CdS branch-like heterostructures with enhanced photostability and photocatalytic activity, *J. Mater. Chem. A* 2 (2014) 2578.

[41] H. Zhou, L. Ding, T. Fan, J. Ding, D. Zhang, Q. Guo, Leaf-inspired hierarchical porous CdS/Au/N-TiO<sub>2</sub> heterostructures for visible light photocatalytic hydrogen evolution, *Appl. Catal. B: Environ.* 147 (2014) 221–228.

[42] L. Ding, H. Zhou, S. Lou, J. Ding, D. Zhang, H. Zhu, T. Fan, Butterfly wing architecture assisted CdS/Au/TiO<sub>2</sub> Z-scheme type photocatalytic water splitting, *Int. J. Hydrogen Energy* 38 (2013) 8244–8253.

[43] J. Zhang, Y. Wang, J. Jin, J. Zhang, Z. Lin, F. Huang, J. Yu, Efficient visible-light photocatalytic hydrogen evolution and enhanced photostability of core/shell CdS/g-C<sub>3</sub>N<sub>4</sub> Nanowires, *ACS Appl. Mater. Interfaces* 5 (2013) 10317–10324.

[44] Quantum Dot Solar Cells Harvesting Light Energy with CdSe Nanocrystals Molecularly Linked to Mesoscopic TiO<sub>2</sub>, 2006.

[45] J.H. Bang, P.V. Kamat, Solar cells by design: photoelectrochemistry of TiO<sub>2</sub> nanorod arrays decorated with CdSe, *Adv. Funct. Mater.* 20 (2010) 1970–1976.

[46] D. Liu, P.V. Kamat, Photoelectrochemical behavior of thin cadmium selenide and coupled titania/cadmium selenide semiconductor films, *J. Phys. Chem.* 97 (1993) 10769–10773.

[47] A. Martínez-de la Cruz, U.M.G. Pérez, Photocatalytic properties of BiVO<sub>4</sub> prepared by the co-precipitation method: degradation of rhodamine B and possible reaction mechanisms under visible irradiation, *Mater. Res. Bull.* 45 (2010) 135–141.